Dalton Transactions



PAPER



Cite this: *Dalton Trans.*, 2022, **51**, 8425

Electron transport through a (terpyridine) ruthenium metallo-surfactant containing a redox-active aminocatechol derivative †

Samudra Amunugama, ^a Eyram Asempa, ^b Ramesh Chandra Tripathi, ^c Dakshika Wanniarachchi, ^t ^a Habib Baydoun, § ^a Peter Hoffmann, ^c Elena Jakubikova ^b * ^b and Cláudio N. Verani ^b *

Aiming to develop a new class of metallosurfactants with unidirectional electron transfer properties, a (terpyridine) ruthenium complex containing a semiquinone derivative L^2 , namely $[Ru^{III}(L^{terpy})(L^2)Cl]PF_6$ (1), was synthesized and structurally characterized as a solid and in solution. The electronic and redox behaviour of 1 was studied experimentally as well as by means of DFT methods, and is indicative of significant orbital mixing and overlap between metal and ligands. The complex forms stable Pockels–Langmuir films at the air-water interface and allows for the formation of thin films onto gold electrodes to prepare nanoscale Au|LB 1|Au junctions for current–voltage (I/V) analysis. Complex 1 shows asymmetric electron transfer with a maximum rectification ratio of 32 based on tunnelling through MOs of the aminocatechol derivative.

Received 27th March 2022, Accepted 12th May 2022 DOI: 10.1039/d2dt00938b

rsc.li/dalton

Introduction

Electron transport in E_1 |molecule| E_2 junctions is measured by the changes in current (I) associated with varying the potential (V) in I/V curves, and is described in terms of conduction, rectification, or insulation. Frequently used metal complexes in electron transport include modified ferrocenes, phthalocyanins, porphyrins, and polypyridines. Metal-terpyridines are often used in both single-molecule or thin film junctions. The pioneering work of Park $et\ al.^2$ observed the conducting behavior of $^{HS}3d^7$ [Co II (S-terpy) $_2$] species where electron transport was observed as a sigmoidal I/V curve attributed to the $^{HS}3d^7$ Co $^{II}/^{LS}3d^6$ Co III redox couple. Coupling between the metal center and the gold electrodes was controlled by the length of alkyl chain spacers between the terpyridine and a self-assembling thiol; while a complex with pentacyl spacers showed an increased resistance that prevented current flow associated

with small bias voltages (Coulomb blockade), another Cocomplex with a thiol directly installed on the terpy showed a sudden temperature-dependent increase in current (Kondo effect). Interestingly, when a $^{\rm HS}3d^5$ [Mn $^{\rm II}({\rm S-terpy})_2$] species was studied by van der Zant $et~al.^3$ ligand reduction triggered a transition to low spin configuration, $t_{2g}^{\ 3}e_g^{\ 2} + e^- \rightarrow t_{2g}^{\ 6}e_g^{\ 0},$ resulting in spin blockade. In these quasi-octahedral 3d species, the filling of t_{2g} HOMOs led to current blockades even if the LUMO e_g -manifold was empty. The HOMO/LUMO gap in 4d metal complexes is wider than that in 3d systems, 4 and when Lee $et~al.^5$ used a $^{\rm LS}4d^6$ [Ru $^{\rm II}(terpy)_2$] system, negative bias switching enabled electron transport by bringing a ligand-based LUMO closer to the Fermi level of the Au substrate. 6

In these cases, the metal-terpy species acted as wires or transistors with electrons flowing back and forth between electrodes, but not as rectifiers. Rectification or unidirectional tunneling of electrons is characterized by asymmetric I/V curves that differ from the sigmoidal I/V response seen for the above examples. In order to attain such rectifying behavior with terpy units, Lacroix et al.7 coupled a naphthalenediimine acceptor (A) through a phenyl bridge to Ru(terpy)2, which acts as a donor (D). In doing so they built a classic Aviram/Ratner/ Metzger $E_1|D-\pi-A|E_2$ design, in which the preferred electron flow is donor → acceptor.8 Although the mechanism of rectification was not pursued, these systems usually rely on e_o-like LUMO tunneling.⁵ We addressed the issue of 3d⁶-induced blockades in quasi-Oh species by building Au|LB|Au junctions based on Langmuir Blodgett films of metallosurfactants containing five-coordinate HSFeIII (3d5, S = 5/2) ions.1 Electron transport takes place through the SOMOs $(d_{xz} + d_{yz})$ when

^aDepartment of Chemistry, Wayne State University, Detroit, MI 48202, USA. E-mail: Claudio.verani@wayne.edu

^bDepartment of Chemistry, North Carolina State University, Raleigh, NC 27695, USA. E-mail: ejakubi@ncsu.edu

^cDepartment of Physics and Astronomy, Wayne State University, Detroit, MI 48201, USA. E-mail: Hoffmann@wayne.edu

[†] Electronic supplementary information (ESI) available. CCDC 2156733. For ESI and crystallographic data in CIF or other electronic format see DOI: https://doi.org/10.1039/d2dt00938b

[‡]Current address: Department of Chemistry, University of Kelaniya, Kandy Road, Dalugama, Kelaniya, 11600, Sri Lanka.

 $[\]$ Current address: BISSELL Homecare Inc., 2345 Walker Ave NW, Grand Rapids, MI-49544, USA.

within 1 eV from the Fermi level of the electrodes. ⁹ The semi-occupied nature of these orbitals limits the amplitude of the current response due to Pauli's exclusion, but precludes the limiting $^{\rm LS}(t_{\rm 2g}{}^6e_{\rm g}{}^0)$ configuration when the metal center is momentarily reduced to 3d 6 Fe $^{\rm II}$ during electron transport. The rectification process has been verified independently, 10 and other SOMO based rectifiers have been identified. 11

This observation led us to consider that tunneling in terpy systems depends on the energies of LUMO, 12 and HOMO 13 as determined by the quasi- O_h environment, as well as on terpy reduction. Therefore, we hypothesize that species in which O_h symmetry is further lifted by the presence of distinct donors and bond lengths will promote significant orbital mixing between metal- and ligand-based molecular orbitals, and may lead to affordable pathways for tunneling.

In order to investigate this possibility, we identified the terpy-based complex $[Ru^{\rm III}(L^{\rm terpy})(L^2)Cl]PF_6$ (1) shown in Scheme 1, in which $L^{\rm terpy}$ is an amphiphilic terpyridine ligand, and the $4d^5$ $Ru^{\rm III}$ ion is bound to a deprotonated and redox-active aminocatechol derivative $L^2.$ Here, we report on the electronic, electrochemical, and rectifying properties of this species, and discuss possible mechanisms.

Results and discussion

Rationale for the molecular design

In our attempt to attain directional electron transport by modulating frontier molecular orbital energy, we propose that the use of redox-active species and asymmetries will lead to significant orbital mixing and overlap. This enables a better match between molecular orbitals and the Fermi level of the electrodes, to foster electron tunneling. The bidentate aminocatechol ligand employed in this study increases the asymmetry of the entire system, possibly aiding in unidirectional electron transport.

Synthesis and characterization

The tridentate 4'-(4-octadecyloxyphenyl)-2,2':6',2"-terpyridine ligand (L^{terpy}) and the redox active 2,4-di-tert-butyl-6-(phenyla-

Scheme 1 Schematic representation of complex 1.

mino)phenol ligand (H₂L²) were synthesized following procedures adapted from literature. 14 Complex 1 [Ru(Lterpy)(L2)Cl] PF₆ was prepared by dropwise addition of one equivalent H₂L² to a methanolic solution of Ru(L^{terpy})(DMSO)₄Cl₂ using triethylamine as the base for phenol and (possibly amine) deprotonation. The synthesis was performed under anaerobic conditions and the reaction system was treated with excess NH_4PF_6 to precipitate the final product as a complex salt. Complex 1 was meticulously characterized by Fourier-transform infrared (FT-IR), 1D and 2D ¹H NMR and ¹³C NMR, UVvisible, and HD-ESI mass spectroscopy analysis. The HD-ESI mass spectrum of 1 showed a signature peak cluster at 1009.47 corresponding to the monovalent [Ru(L^{terpy})(L²)Cl]⁺ ion. A diagnostic isotopic envelope was observed, confirming the presence of all expected isotopes, including seven stable ruthenium and two chloride isotopes. The complex formation was further validated by the presence of distinct vibrational modes in the FT-IR spectrum, particularly, strong bands observed at 2924–2853, 1584–1516 and 846 cm⁻¹ respectfully attributed to C-H, C=C, and P-F stretches.

Molecular structure in the solid state

In spite of several attempts, the crystal structure for complex [Ru(L^{terpy})(L²)Cl]PF₆ 1 was not obtained. However, we solved the structure of an analogue displaying a shorter -OC9H19 alkoxy chain, as illustrated in Fig. 1, with selected data reported in Table T1.† The complex shows pseudo-octahedral geometry around the ruthenium center, with L^{terpy} occupying the meridional plane. Two geometrical isomers are possible for this complex depending on the position of the -N-phenyl portion and O atoms of L² in regard to the Cl group. 15 However, the crystal structure of this analogue indicates that the -N-phenyl group is preferentially oriented trans to the Cl atom in its favored thermodynamic product. Bond length between ruthenium and the central nitrogen atom, N1, of the terpyridine ligand is shorter (1.972 Å) than the other two Ru- $N_{terpyridine}$ bonds at 2.073 Å, 2.068 Å due to steric effects. ¹⁶ The observed Ru-N_{terpy} bond lengths are in excellent agreement with literature reported values of similar compounds. 14a,17 Moreover, the bond lengths between ruthenium and the O-

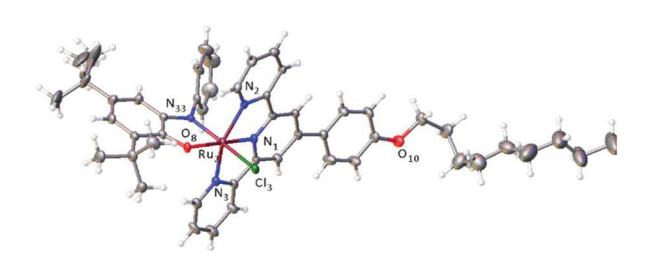
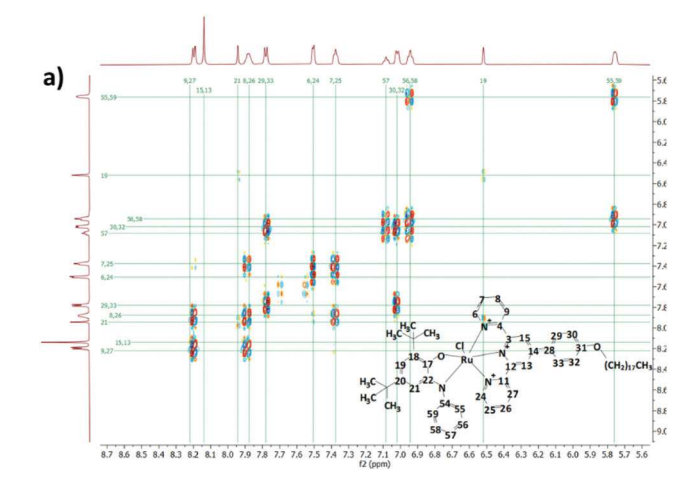


Fig. 1 X-ray crystal structure of the [Ru(L^{terpy})(L²)Cl]PF₆ (CCDC 2156733†) analogue displaying a shorter $-OC_9H_{19}$ alkoxy chain at 50% probability; the PF₆ counter ion is omitted for clarity. Selected bond lengths: Ru–N1 = 1.972(2), Ru–N2 = 2.073(3), Ru–N3 = 2.068(3), Ru–O8 = 2.0365(19), Ru–N33 = 1.971(2), Ru–Cl = 2.3875(7), C–N_{average} = 1.394, C41–O8 = 1.281, C–C_{average} = 1.4310 Å.

and N-atoms of the aminocatechol ligand reach Ru-O8 = 2.0365 Å and Ru-N33 = 1.971 Å. The Ru-Cl bond distance of 2.3875 Å is comparable to the values reported by Lahiri et al., 18 further implying that the -N-phenyl group is trans to Cl⁻. The average C-C bond values reach 1.431 Å, while the specific distances of relevance are 1.281 and 1.347 Å for bond lengths of C41-O8 and C40-N33, respectively. When compared with literature reported bond lengths of similar species the structure of this analogue for complex 1 has bond length characteristics between those of structures for [RuIII-semiquinone] and [Ru^{II}-quinone], 15,19 and the assignment of the nature of L² in 1 on the basis of the solid structure of its derivative is not straightforward. However, lack of a proton in N33, allied to a careful analysis of bond lengths in other systems, 14b,c,20 strongly suggests the presence of a [Ru^{III}semiquinone].

Molecular structure in solution

Ligands and complex 1 were characterized by ¹H NMR and ¹³C NMR nuclear magnetic resonance in deuterated dichloromethane (CD₂Cl₂). The well-resolved peaks in the ¹H NMR spectrum reinforces the description of species 1 as containing a 4d⁵ Ru^{III} metal center magnetically or electronically coupled to a semiquinonoid L2 in a distorted octahedral field. The 1H NMR of H₂L² shows two broad singlets with an intensity of 1 proton, which are assigned to OH and NH groups. These peaks are absent in the NMR spectrum of the metal complex indicating that the ligand is bound to the metal through these deprotonated functional groups. The aromatic region of the ¹H NMR of 1 displays 12 signals corresponding to 21 protons. These signals are fully assigned based on coupling patterns exhibited in correlation spectroscopy (COSY) and heteronuclear single-quantum correlation spectroscopy (HSQC) data. COSY data indicate the interactions between nearby protons in the structure while HSQC experiment is used to determine the direct correlation between ¹H and ¹³C atoms. Fig. 2(a) and S5† show aromatic region of COSY and HSQC for complex 1 respectively. Although there are two possible geometrical isomers for 1 associated with the relative position of the aminocatechol and chlorido ligands, 15 1H NMR revealed the presence of only one species as the favoured thermodynamic product. This further validates the exclusive observation of the trans-species of derivative of 1 in the X-ray crystal structure. Upon coordination to the metal center, most of the protons of terpyridine ligand L^{terpy} show a slight upfield effect, yet protons # 6 and 24 indicate a significant upfield shift compared to the free ligand. This is explained by considering the configuration of the molecule where the terpyridine is perpendicular to L² causing protons # 6 and 24 of L^{terpy} to be above the aromatic plane of the amino-catechol ligand which increase the shielding effect. Similarly, protons # 55 and 59 of L² also exhibited a characteristic shielding effect in the metal complex relative to the uncoordinated ligand.²¹ This upfield peak positions of protons # 6, 24, 55, and 59 in 1 suggest a preferential trans arrangement of the -N-phenyl portion of L² with respect to the Cl group. 22 As available in the Experimental



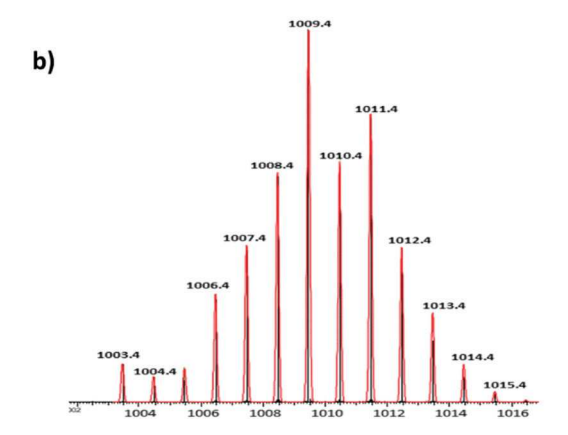


Fig. 2 Analyses for complex 1, (a) COSY NMR spectrum of the aromatic region in CD_2Cl_2 . (b) High resolution ESI-mass spectrum, the black bars show the experimental spectrum and the red continuous trace indicate the simulated spectrum.

section, the peak distribution for ¹H NMR compares well with the expected peak pattern and the COSY spectrum also exhibit the predicted correlations. In the aromatic region of the COSY spectrum, peaks at 6.51 ppm (# 19) and 8.14 ppm (# 15,13) do not show any correlation to other peaks. The aromatic protons # 30,32 and 29,33 of the phenyl ring attached to terpyridine show correlation to each other, as expected. Additionally, the protons # 8 and 26 of the terpyridine exhibit coupling to both the protons #7, 25 and #9, 27 in the COSY spectrum, whereas the protons # 7 and 25 also show correlation peaks with protons # 6 and 24. The hydrogen atoms # 56 and 58 in the phenyl ring attached to the aminocatechol demonstrates interactions with protons # 55, 59 and 57. Significant coupling between protons can be observed in the aliphatic region of the COSY spectrum due to the presence of 17 -CH₂ groups. Hence, the 1D and 2D NMR spectroscopy data confirm the expected structure for complex 1.

Electronic structure

The UV-visible spectroscopy data for complex 1 was recorded in dichloromethane using a 10^{-4} M solution (Fig. S7†) in an

attempt to determine the electronic structure of 1 and the nature of the aminocatechol derivative. Complex 1 shows intense absorption bands in the UV region around 230, 284 and 320 nm corresponding to $\pi \to \pi^*$ intraligand (IL) transitions. 15,23 The strong absorption band observed in the visible region at 577 nm ($\varepsilon \approx 24\,500~\text{M}^{-1}~\text{cm}^{-1}$) can be attributed to a metal to ligand charge transfer (MLCT) transition,²⁴ whereas the broad band at around 1070 nm ($\varepsilon \approx 410 \text{ M}^{-1} \text{ cm}^{-1}$) is tentatively identified as either a d-d transition or a low intense MLCT transition. Final assignment will rely on TD-DFT calculations. The MLCT electronic transitions are governed by interactions between the highest occupied molecular orbitals (HOMOs) and lowest unoccupied molecular orbitals (LUMOs) of the complex, 24c,25 and their attribution have been the topic of intense debate because both the metal and the ${\rm L}^2$ derivative can attain several redox states. Ruthenium can either be LS4d⁶ Ru^{II} or LS4d⁵ Ru^{III}, whereas L² can exist in its protonated and reduced aminocatecholoid (AC), oxidized and deprotonated semiguinonoid (SO) or fully oxidized and deprotonated quinonoid (Q) form. On the one hand, Fujita et al. 19a and Lahiri et al. 15 did extensive studies on similar [Ru(terpy) (iminobutylQ)Cl]⁺ and [Ru(terpy)(iminobenzoQ)Cl]⁺ complexes, respectively. Their contributions suggest considerable mixing of Ru $(d\pi)$ and amino catechol derivative (π^*) orbitals with significant contributions from both Ru^{II}-quinone (O) and Ru^{III}-semiquinone (SQ) resonance forms. Mixing of orbitals yields a highly delocalized molecular structure. 19a,b,26 The peak in the visible region which dominates the UV-visible spectrum of these complexes was assigned as a transition from a molecular orbital with metal character to an aminocatecholbased MO, namely $t_{2o}(d_{yz}) \rightarrow \pi^*$, by Fujita and co-workers. ^{19a} Even though this absorption band is presented as a MLCT transition, this is a simplification as contributions from distinct metal- and ligand-based MOs make it a ML-to-LM transition. Furthermore, they suggest that frontier molecular orbitals are comprised of destabilized Ru $t_{2g}(d_{xy})$ and $d_{x^2-y^2}$ orbitals and π/π^* orbitals of the aminocatechol derivative, with only minor contributions from Cl ligand. We have observed similar orbital mixing in other metallosurfactants with bipyridineruthenium(II) and redox-active ligands.²⁷ On the other hand, Lahiri and co-workers¹⁵ interpret these electronic transitions differently. According to experimental data and complementary theoretical calculations, the most intense transition in the visible region was assigned as an electron transfer $Ru(d\pi) + Cl$ $(\pi) \to \pi^*(\text{terpy})^{28}$ With the d π MO necessarily belonging to the t_{2g} manifold in an O_h point group, the authors refrain from a more specific attribution. Nonetheless, this attribution assumes that the ground state of the [Ru(terpy)(iminobenzoQ) Cl]⁺ complex entails a trivalent and spin-coupled singlet 4d⁵ Ru^{III}-SQ form with minor contributions from the Ru^{II}-Q state. Finally, to increase complexity, the characteristic broad band that appear in the near IR region has been identified as a transition $Ru(d\pi) \to \pi^*(SQ)$ by a classic treatment of orbital mixing in ruthenium/quinone ligands by Lever and coworkers, 24c ergo within the t_{2g} manifold again. However, the molar extinction coefficient of the observed band in 1 is significantly less intense than the value observed for the $Ru^{II} \rightarrow \pi^*$ (SQ) transition; hence, it can be described as a d-d band. While the peak positions and intensities of electronic spectrum for 1 correlates well with Fujita's observations, we thought prudent to conduct our own DFT calculations, in correlation with the redox properties of complex 1, as recorded in dichloromethane using TBAPF₆ as the supporting electrolyte and illustrated in Fig. 3. The cyclic voltammogram of 1 revealed a rich electrochemical response attributed to four redox processes within the experimental potential range of $\pm 1.80~V_{Ag/AgCl}$ (at an equivalent +1.30 and -2.30 V_{Fc/Fc+}). The first reversible process occurred at +1.26 $V_{Ag/AgCl}$ (+0.76 $V_{Fc/Fc+}$, $\Delta E = 0.09 V$, $|i_{pa}/i_{pc}| =$ 1.18), while the other processes were observed respectively at $-0.25 \text{ V}_{Ag/AgCl} \left(-0.76 \text{ V}_{Fc/Fc+}, \Delta E = 0.07 \text{ V}, |i_{pa}/i_{pc}| = 0.95\right), -1.10$ $V_{Ag/AgCl}$ (-1.60 $V_{Fc/Fc+}$, $\Delta E = 0.07$ V, $|i_{pa}/i_{pc}| = 1.11$) and -1.74 $V_{
m Ag/AgCl}$ (-2.22 $V_{
m Fc/Fc+}$). Even though this redox behavior is typical for ruthenium polypyridine complexes with similar redox-active ligands, relating these redox states with electronic forms of the molecule is challenging. Hence, similar to the previous section, distinct groups have interpreted these processes differently.²⁹ Fujita and co-workers^{19a,26} suggest that the ground state of [Ru(terpy)(iminobutylQ)Cl]⁺ favors Ru^{II}-Q form, based on theoretical calculations, experimental UVvisible and spectro-electrochemical studies. Consequently, the first process observed for their system at 1.17 V_{Ag/AgCl} was assigned to the Ru^{II}/Ru^{III} couple and the process at -0.21 V_{Ag/AgCl} as Q/SQ couple. However, based on EPR and DFT calculations, Lahiri et al. 15 proposes an alternative assignment in which these processes are all metal-based. The electrochemical potentials observed for our complex 1 are comparable to the values reported by Lahiri et al., 15 and together with 1H NMR, mass spectroscopic and UV-visible spectroscopic analysis, this suggests that [Ru(L^{terpy})(L²)Cl]PF₆ (1) has similar Ru^{III}-SQ characteristics. This is also supported by the X-ray structure of the derivative of 1. Thus, the first positive process at +1.26 V_{Ag/AgCl} can be assigned to the Ru^{III}/Ru^{IV} redox couple, whereas the next two processes are attributed to reduction of the L² ligand from aminosemiquinone to aminocatechol and to the

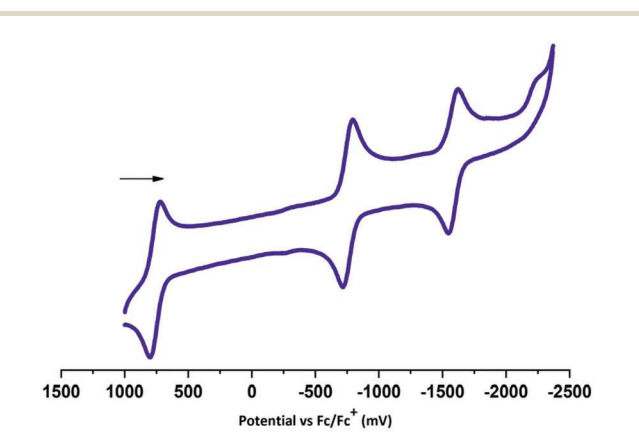


Fig. 3 Cyclic voltammogram of complex 1 in 1×10^{-3} M DCM. Glassy carbon as working electrode, Ag/AgCl as reference electrode, Pt wire as auxiliary electrode, and 0.1 M TBAPF₆ supporting electrolyte.

Ru^{III}/Ru^{II} couple, respectively. The most reduced peak is ascribed to a terpyridine-based process.

DFT calculated structure

DFT calculations at the B3LYP-D3/SDD,6-311G* level were used to evaluate the nature and energies of the frontier molecular orbitals in compound 1 to provide insight into the observed electronic and electrochemical results, and to serve as basis to discuss electron transfer. The -O(CH₂)₁₇CH₃ alkoxy group in 1 was replaced with a -OCH3 group for the simplicity of calculation. Removal of this group is not expected to affect the electronic properties of the calculated molecules. Two different models were considered, namely a singlet and a triplet ground state configuration. Our calculations identify the most stable ground state for complex 1 as the singlet state (LS4d RuIIISQ $(\uparrow\downarrow)$, being favourable by 10.60 kcal mol⁻¹ over the triplet spin state Ru^{III}SQ(↑↑). Furthermore, an excellent correlation was attained between the metal-ligand bond lengths and angles in the crystal structure of 1 and that of the calculated singlet ground state, suggesting the presence of a LS4d5 Ru(III) metal center coupled with the unpaired electron of SO ligand. The calculated Ru-O8 and Ru-N33 bond lengths reach 2.07 and 1.98 Å and therefore are slightly longer than the observed experimental values by 0.03 and 0.01 Å, whereas the Ru-Cl bond is calculated at 2.42 Å, thus 0.03 Å longer. A detailed analysis of theoretical and experimental bond lengths is provided in Table T3 (see ESI†). Interestingly, in spite of multiple attempts, a purely antiferromagnetically coupled Ru^{III}-SQ state did not converge to a minimum using B3LYP-D3. This is similar to the calculations performed by Fujita et al. 19a This observation implies that the Ru^{III}-SQ species is electronically coupled; a simplified scheme can be drawn in which the singly-occupied SQ π orbital strongly interacts with a singlyoccupied RuIII t2g orbital, generating a bonding and an antibonding combination (see HOMO-3 and LUMO in Fig. 4). The resulting bonding MO is doubly-occupied, while the antibonding MO is unoccupied. In fact the picture is more complex with contributions of terpy and Cl orbitals. Fragment orbital analysis was performed to quantify the frontier molecular orbital localization on the metal and different ligands in the singlet state of 1. There are four fragments used in this study namely, Ru, terpyridine, catechol and chloride. As expected for a standard polypyridine complex, the main contribution for occupied molecular orbitals in 1 comes from the $Ru_{d\pi}$ orbitals, or the t_{2g} (d_{xy^2} , d_{xz^2} , d_{yz^2}) subset of a quasi-O_h simmetry.²⁷ Specifically, the HOMO, HOMO-1 and HOMO-3 orbitals show about 47-60% localization on the metal ion with minor contributions from the orbitals in the chloride and terpyridine ligands. While the HOMO and HOMO-1 show π -donor interactions between the Cl and Ru, HOMO-3 displays a π -bonding interaction between the Ru and the aminocatechol derivative, suggesting that L^2 acts as a π -acceptor in this system. Interestingly, the HOMO-2 orbital in 1 consists mainly of a terpy-based molecular orbital, emphasizing the extension of orbital mixing in this system. The LUMO is predominately located on the aminocatechol derivative with a significant con-

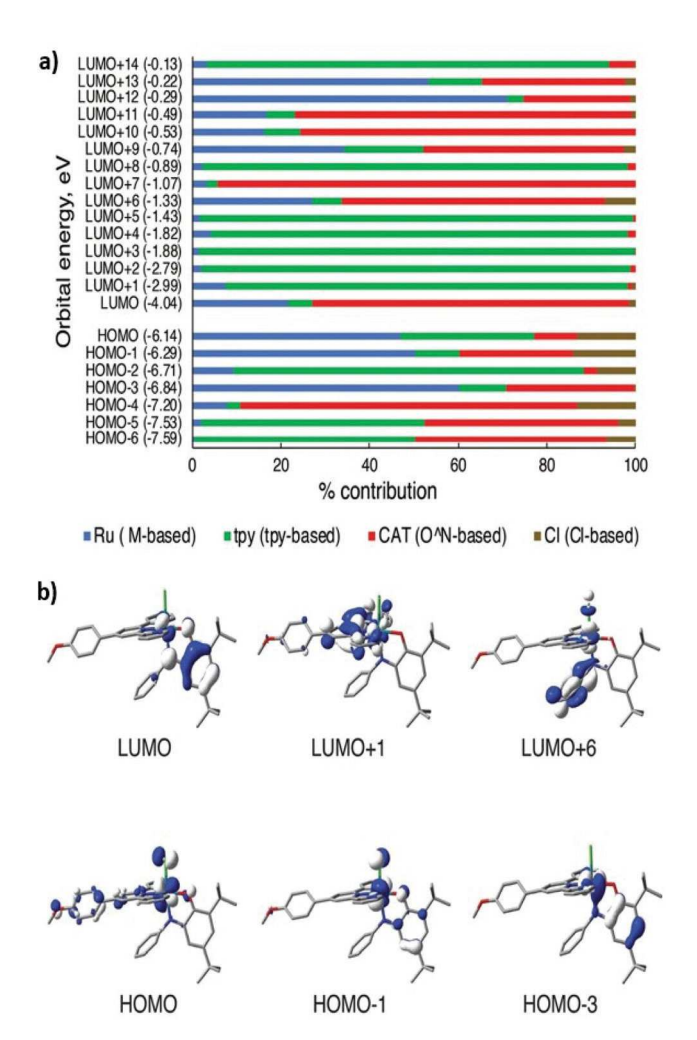


Fig. 4 (a) Calculated molecular orbital energy diagram for complex ${f 1}$. (b) Frontier molecular orbitals for singlet state of ${f 1}$.

tribution (~20%) from Ru, while LUMO+1 through LUMO+5 are predominantly terpy-based with 91–98% electronic contribution. The orbital diagram with percent composition of molecular orbitals shown in Fig. 4. Indicate that complex 1 exhibits significant overlap between Ru($d\pi$), terpy and L² orbitals.

Correlation of calculations to electronic and redox data

DFT methods were used to obtain the UV-visible and oxidation/reduction potentials of 1 in solution. The resulting electronic properties showed comparable features with the experimental data, with one intense absorption band in the visible region and one in the near-IR region (Fig. S13†). The calculated UV-visible spectrum exhibit a systematic hypsochromic shift of 0.1–0.2 eV relative to the experimental spectrum. The theoretical spectrum displays peaks at 527 and 981 nm, which correlate with experimental peaks at 577 and 1070 nm. The intense absorption band in the visible region includes a complex MLCT (Ru(d π) \rightarrow terpyridine/aminocatechol ligand) and ligand to ligand (LL) charge transfer transition ($\pi \rightarrow \pi^*$) localized on the amino catechol ligand. The peak in the near-

IR region is composed of two main hole-particle pairs that display MLCT from $Ru(d\pi)\to\pi^*$ of amino catechol-based ligand and LL charge transfer based on amino catechol ligand. The tentative experimental attribution to a d-d process was not observed. Theoretical analysis of redox properties suggests good correspondence between calculated and experimental potentials for the first cathodic and first anodic peak potentials with a difference of 0.05 and 0.15 $V_{\rm Fc/Fc+}$ respectively. Nonetheless the calculated second and third cathodic redox potentials show a respective difference of 0.60 and 0.80 $V_{\rm Fc/Fc+}$ from the experimental peaks. This is due to the fact that the calculated redox potentials did not account for the proton transfer that is expected to be coupled with the second and third cathodic potentials.

Interfacial behavior and film formation

In order to build the Au|LB|Au junction that enables the study of electron transfer properties for complex 1, it is necessary to study the behavior of molecular monolayer films at the air water and air solid interface. The presence of tert-butyl and alkyl groups give a hydrophobic nature to this complex. Yet, the polar and charged nature of the ruthenium lends hydrophilicity that makes 1 a practical redox-active surfactant to enable the deposition of Langmuir-Blodgett monolayers. The surface properties of [Ru(L^{terpy})(L²)Cl]PF₆ (1) were initially evaluated by compression isotherm and Brewster angle microscopy (BAM), as shown in Fig. 5 and the complex forms a stable Pockles-Langmuir monolayer³⁰ at the air|water interface with a collapse pressure of 37 mN m⁻¹. An approximate critical area for 1 was calculated using the parameters provided by the X-ray crystal structure in Fig. 1, and is estimated at about 80-85 Å². This value is in good agreement with the experimentally observed critical area of 77 Å², which is indicative of formation of a compact monolayer at the air-water interface. Furthermore, BAM images exhibit collapse as an array of

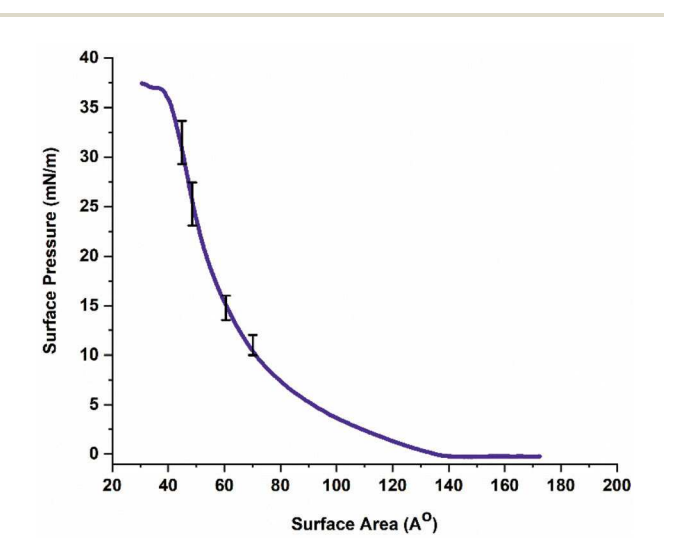


Fig. 5 Compression isotherm for complex 1. The vertical error bars display limits over three compression experiments.

Newton rings occurring due to multilayer formation after the collapse of the monolayer. The Langmuir-Blodgett films were structurally characterized by infrared reflection absorption spectroscopy (IRRAS), UV-visible spectrometry, and electrospray ionization mass spectrometry (ESI-MS) methods. Although the molecular devices are built with monolayers, spectroscopic analysis of a monolayer cannot be completed accurately due to the detection limit of instruments. Therefore, we used a sample with 57 monolayers of complex 1 for IRRAS and UV-visible measurements. Langmuir-Blodgett monolayers of [Ru(L^{terpy})(L²)Cl]PF₆ (1) were transferred onto glass, mica, or gold substrates Y-type dipping with a head-head and tail-tail configuration. A constant pressure of 27 mN m⁻¹ was maintained during the deposition at 23 °C. The IRRAS method uses polarized light at a specific angle to obtain the vibrational peak patterns of the deposited thin film.³¹ A comparison between IR spectrum of the bulk sample and the IRRAS spectrum of the film recorded at p-polarized light at an incident angle of 30° is shown in Fig. 6. The IRRAS spectrum of the LB film shows good agreement with the bulk IR spectrum of the complex and exhibits equivalent peak positions. The symmetric and asymmetric stretching vibrations related to -CH2 groups of the long alkyl chain appear at 2924, 2842 cm⁻¹ respectively. The shift of -CH₂ stretching frequencies suggest a condensed and well-ordered film formation with preferential all-trans confirmation in alkyl chain.31,32 Stretching frequencies corresponding to -CH3 groups in the bulk sample are observed at 2956 cm⁻¹, and shift to 2965 cm⁻¹ in the LB film suggesting that the alkane chains are somewhat tilted with respect to the surface. Prominent peaks observed between at 1600 and 1300 cm⁻¹ are attributed to aromatic C=C, C=N stretching and CH₃/CH₂ bending vibrations, and indicative that the aromatic ligand remains intact after deposition onto

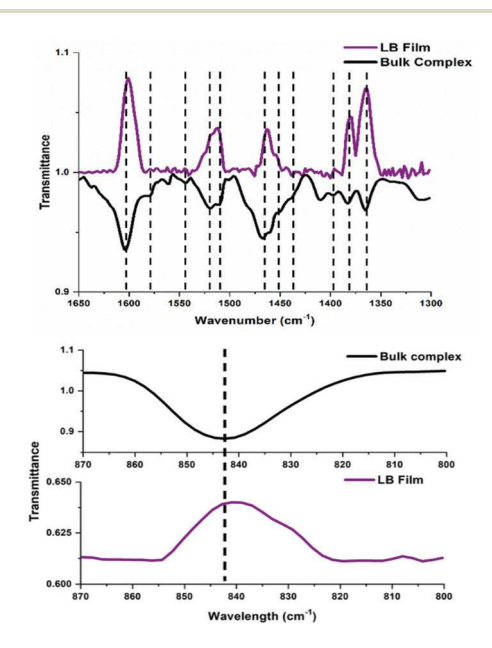


Fig. 6 Comparison of IRRAS spectrum of 57 layers of LB film and IR spectrum of complex **1**.

solid substrates. Furthermore, the vibration of the PF₆ counterion appears at 840 cm⁻¹ for the deposited thin film. The presence of positive (upward) and negative (downward) peaks in the IRRAS is explained by surface selection rules.³³ A positive peak is observed for a functional group that has a surface-perpendicular transitional dipole moment with respect to the dielectric substrate, whereas the surface-parallel component of a transition moment yields a negative band in the IRRAS spectrum.33,34 The UV-visible spectrum of the LB film of complex 1 shows excellent agreement with the bulk UV-visible spectrum, as shown in Fig. S10† and the general spectral characteristics were preserved, including the MLCT band that occurs at 581 nm. The slight red shift observed is attributed to aggregate formation in the multilayer arrangement.³⁵ The LB films deposited on glass substrate were scraped off and further analysed via ESI-MS. The mass spectroscopy data confirmed that the bulk [Ru(L^{terpy})(L²)Cl]PF₆ (1) and multilayer LB films exhibit similar isotopic distribution and m/z value (Fig. S10(b)†).

LB film deposition and morphological analysis

LB monolayers of the complex were deposited at different surface pressures and analysed by Atomic Force Microscopy (AFM) images. To ensure complete transfer of the film on the substrate, the transfer ratio was maintained near unity. As shown in Fig. 7(a), the AFM analysis indicates that the films deposited at the low surface pressure of 17 mN m⁻¹ have a higher number of pin hole defects, whereas films deposited above 30 mN m⁻¹ pressure exhibit significantly rougher surfaces indicative of aggregate formation. Monolayers deposited between 22 and 27 mN m⁻¹ display a smoother film surface and were further considered. The thickness of a monolayer film of 1 was determined by blade-scratching method using quartz substrates with nine to fifteen layers. These films were scratched, and the depth of the resulting trench was measured using AFM in the contact mode. The resulting values yield a linear relationship between the thickness and the number of layers, which indicates homogeneous film deposition. The plotting of layer thickness vs. layer number shown in Fig. 7(b) indicates an average thickness of ca. 30-32 Å per monolayer. Using the parameters from the crystal structure for comparison, the approximate length of compound 1 can be estimated at ~43 Å. However, due to the presence of hydrophobic and flexible groups at both ends of the molecule, we assume that the terpyridine moiety lies nearly flat on the surface. Rather than in a linear configuration, both t-Bu and alkyl groups bend out of the surface plane. The film thickness reflects this non-liner arrangement.

Fabrication of Au|LB|Au junctions

The monolayer of compound 1 was deposited on a pre-cleaned gold substrate (Au_1 , bottom) at a surface pressure of 27 mN m⁻¹, and dried in a desiccator for five days under reduced pressure. The top gold electrode (Au_2) was deposited using shadow masking³⁶ with an Effa-Coater gold sputter. Four assemblies containing 16 individual $Au_1 \mid LB1 \mid Au_2 \mid$ junctions

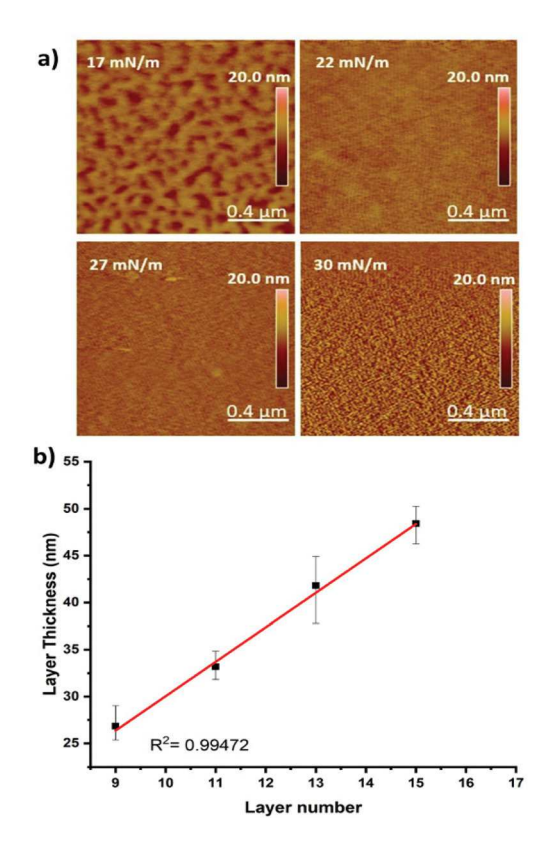


Fig. 7 (a) AFM images of monolayers of complex 1 deposited on mica substrates at different surface pressures. (b) Graph of layer thickness *versus* number of layers of complex 1.

were prepared, yielding a total of 64 junctions to be analyzed for their current–voltage (I/V) characteristics at room temperature using a Keithley 4200 semiconductor parameter analyzer connected to a Signatone S-1160 Probe Station.

Feasibility and observation of electron transport

For electron transport to happen it is necessary that the energies of the electrodes and the molecule are compatible. Therefore, knowing that the gold electrode displays Fermi levels at -5.1 eV below the vacuum level, $^{5,9}d,^{37}$ we convert the reduction and oxidation potentials of complex 1, obtained via cyclic voltammetry, to assess the solid-state energies associated with the frontier molecular orbitals of the molecule. The experimental potentials measured vs. Ag/AgCl are transformed into saturated calomel electrode potentials ($V_{\rm SCE}$), and then converted into the first electron affinity ($V_{\rm a}$) and first ionization energy ($V_{\rm i}$) of the molecule as respectively given by the Hipps and Armstrong models: 5,38

$$V_{\rm a} = 4.7 \text{ eV} + E_{1/2}^{\rm red}(\text{SCE})$$
 (1)

$$V_{\rm i} = 4.7 \text{ eV} + (1.7) E_{1/2}^{\rm ox}(SCE)$$
 (2)

These energies are given in eV, and can be considered approximately similar to the respective LUMO and HOMO energies of complex ${\bf 1}$. As such, the LUMO of the complex

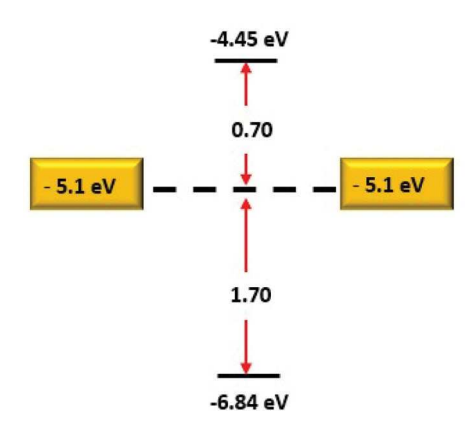


Fig. 8 Frontier molecular orbital energy values (from CV data) for complex **1** compared with Fermi energy of gold electrodes.

is at -4.45 eV or 0.7 eV above gold, whereas the HOMO energy level is about 1.7 eV below (Fig. 8). The excellent match within 1 eV between LUMO and Fermi level suggests that electron transport based on tunnelling through the molecule is feasible.

In order to probe our hypothesis that distortions of the Oh symmetry will lead to significant orbital mixing between molecular orbitals ruthenium, terpy, aminocatechol and chlorido ligand, leading to affordable pathways for tunnelling, we tested electron transport experimentally. We probed the current-voltage characteristics of multiple Au₁|LB1|Au₂ junctions in each assembly by applying a bias voltage to the top electrode while maintaining the bottom gold electrode at zero bias voltage (Fig. 9). Although, due to monolayer defects, ca. 8-10 devices of each assembly were short circuited, an average of 35-40% of devices among four assemblies signify asymmetric electron transfer behaviour with higher current in the negative quadrant of the I/V curve compared to the negligible current response in the positive side. The amplitude of observed current response for 1 is comparable to similar studies reported in the literature, which employed LB films for molecular device preparation. 9a,d,39 This unquestionable direc-

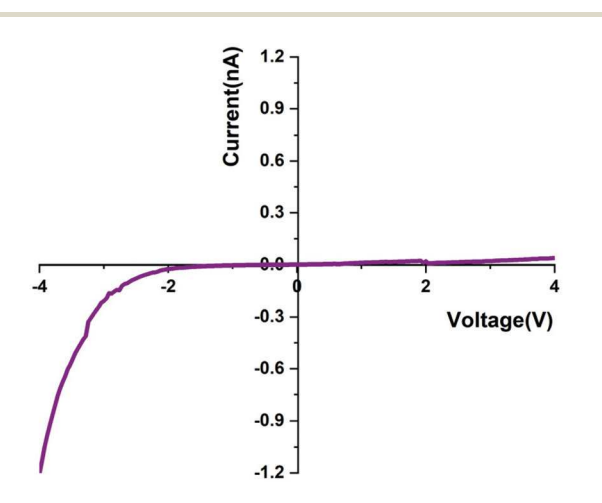


Fig. 9 I/V curve for Au|LB 1|Au molecular junction between ± 4 V.

tional electron transport was further established by the rectification ratio (RR = [I at -V/I at +V]), which varied from 4 to 18 between -2 V to +2 V and from 5 to 32 between -4 V to +4 V. Repetition of measurements on the same device leads to lower currents that tend to display a more sigmoidal I/V behavior. This has been tentatively explained as an effect of molecules to decrease their energy in high electric fields by reorganizing their dipole moments. 8b,9a,38c Compared to similar asymmetric terpyridine-based metal complexes, the I/V characteristics of 1 are analogous to the Ru-based dyad electrografted on gold, studied by Lacroix et al. using Ti/Au as the top electrode. This species showed a substantially large RR of 300 at ±2.5 V. Even though the RR value of complex 1 is smaller, these studies confirm the feasibility of directional electron transfer of 1. Based on the reasonably low LUMO-Fermi energy gap of 0.7 eV and the asymmetric placement of 1 between the top and bottom electrodes, we suggest that directional electron transfer shown in this study likely entails an asymmetric rectification mechanism in which the electrons tunnel through the ligandbased LUMO without necessary involvement of the metalbased HOMOs. It has been shown that incorporation of alkyl chain in the molecule causes an asymmetric displacement of the redox active moiety from the top electrode and leads to a potential drop between alkyl chain and the electrode. 40 Consequently, this asymmetric placement is also regarded as a favorable factor for through-molecule directional charge transport. However, the incorporation of these insulating chains can result in limited transport and blocades, 7,40,41 which may explain the moderate rectification ratios obtained for 1, when compared with other systems. 7,40,42

Conclusions

We have successfully designed and studied a redox-active ruthenium metallosurfactant $[Ru^{III}(L^{terpy})(L^2)Cl]PF_6$ (1) with extensive orbital mixing between the Ru center, the terpy and the semiquinone ligands. The electronic and redox properties suggest that 1 has a low lying LUMO primarily associated with the semiquinone ligand, which can partake in directional electron transport in Au|LB 1|Au junctions. The asymmetric I/V profile of 1 is in distinct contrast with the symmetric response obtained by similar (terpy)M species discussed in this account, and validate our hypothesis that heavily distorted O_h species with distinct donors will enable tunnelling through empty and heavily mixed molecular orbitals. Further studies will examine the effect of temperature and magnetic fields on the observed current and rectification ratio of similar molecular species.

Experimental section

Materials and methods

Reagents and solvents were used as purchased from commercial sources. A Varian 500 MHz instrument was used for ¹H NMR, ¹³C NMR, COSY and HMQC NMR spectra. The Fourier-

transform Infrared spectrum of ligands and the complex were recorded as KBr pellets using a Tensor 27 spectrometer in the range of 4000-400 cm⁻¹. Elemental analysis of complex 1 was performed by Midwest Microlab, Indianapolis, USA. ESI mass spectroscopy data in the positive mode for both the complex and its thin films was acquired using a Waters micromass ZQLC/MS instrument. A UV-3600 Shimadzu spectrophotometer was used to measure UV-visible spectra in the range of 190-1600 cm⁻¹. Cyclic voltammetry experiments were performed using a BAS 50 W potentiostat with a standard threeelectrode cell consisting of a platinum wire auxiliary electrode, glassy carbon working electrode and Ag/AgCl reference electrode. Experiments were conducted under argon at room temperature using TBAPF6 as the supporting electrolyte. All the potentials were referenced according to the potential of ferrocene⁴³ used as the internal stranded.

Syntheses

4'-(4-octadecyloxyphenyl)-2,2':6',2"-terpyridine (L^{terpy}). The terpyridine ligand was synthesized according to the Kröhnke synthesis method. Two equivalents of 2-acetyl pyridine (0.64 mL) was reacted with one equivalent of 4-octadecyloxy benzaldehyde (0.93 g) in the presence of two equivalents of KOH (0.30 g) and NH₄OH (7.36 mL). The reaction mixture was refluxed for 4 h at 60 °C. The off-white product was recrystallized in absolute ethanol to obtain a white color precipitate. Yield (30%). ZQ-MS (m/z^+) = 576.93 (100%) for [C₃₉H₅₁N₃O] (calculated = 577.86). FT-IR (KBr cm⁻¹) 2850–2920 (ν C-H), 1584–1516 (ν C=C, aromatic), 1469 (ν C=N, aromatic). HNMR, ppm (CD₂Cl₂, 400 MHz) δ 8.74 (m, 6H), δ 7.89 (m, 4H), δ 7.38 (t, 2H), δ 7.05 (d, 2H), δ 4.06 (t, 2H), δ 1.83 (t, 2H), δ 1.28 (m, 30H), δ 0.89 (t, 3H).

 ${
m Ru(DMSO)_4Cl_2}$. ${
m RuCl_3\cdot xH_2O}$ (2.00 g), dissolved in DMSO (25 mL) was refluxed at 80 °C until the deep red colour changed to orange. After cooling down to room temperature, acetone (40 mL) was added to the reaction mixture and the final solution was cooled in an ice bath to obtain a yellow precipitate. Yield (80%).

Ru(L^{terpy})(**DMSO**)Cl₂. One equivalent of Ru(DMSO)₄Cl₂ (0.22 g) was reacted with one equivalent of L^{terpy} (0.25 g) in ethanol (20 mL) under dark conditions. The solution was refluxed for 18 h under argon. The crude product was washed with cold ethanol and water and dried under vacuum. Yield (67%). FT-IR (KBr, cm⁻¹) 2922, 2852 (long chain C–H), 1603, 1519, 1467, 1402 (Pyridine rings), 1080 (S=O). ¹H NMR, ppm (CD₂Cl₂, 400 MHz) δ 9.27 (d, 2H), δ 8.19 (d, 4H), δ 7.96 (t, 2H), δ 7.78 (d, 2H), δ 7.63 (t, 2H), δ 7.06 (d, 2H), δ 4.06 (t, 2H), δ 2.75 (s, 6H), δ 1.85 (t, 2H), δ 1.28 (m, 30H), δ 0.89 (t, 3H).

2,4-Di-tert-butyl-6-(phenylamino)phenol (H_2L^2). 2.00 g of 3,5-di-tert-butylcatechol was dissolved in *n*-heptane in the presence of triethylamine (0.12 mL). Then aniline (0.82 mL) was dissolved in n-heptane separately and was added to the 2,4-di-tert-butyl-6-(phenylamino)phenol solution. Final mixture was refluxed for 5 h and then stored at 4 °C to obtain needle-like crystals. Yield (89%). FT-IR (KBr, cm⁻¹) 2961(tert-butyl group C-H), 1600, 1496, 1418, 1363 (Pyridine rings). ¹H NMR, ppm

(CD₂Cl₂, 600 MHz) δ 7.25 (d, 1H), δ 7.20 (t, 2H), δ 7.07 (d, 1H), δ 6.84 (t, 1H), δ 6.67 (d, 2H), δ 6.48 (s, 1H), δ 1.45 (s, 9H), δ 1.28 (s, 9H).

[Ru(L^{terpy})(L²)Cl]PF₆ (1). A mixture of Ru(L^{terpy})(DMSO)Cl₂ (0.40 g) and H₂L² (0.44 g) was refluxed in argon-degassed ethanol for 18 h. The volume of the resultant solution was reduced and NH₄PF₆ (0.10 g) was added. The dark-purple product was isolated and further purification was done by chromatography using neutral alumina with dichloromethane: acetonitrile (9:1). Yield (10%). ZQ-MS(m/z+)1009.4717(100%) for $[C_{59}H_{76}ClRuN_4O_2]^+$ (calculated = 1009.47). FT-IR (KBr, cm⁻¹) 2924, 2853 (long chain C-H), 1603, 1519, 1467, 1383, 1365 (Pyridine rings C=C, C=N), 1243 (t-butyl), 1183 (C-O-C), 843 (PF6). ¹H NMR, ppm (CD₂Cl₂, 600 MHz) δ 8.20 (d, 2H), δ 8.14 (s, 2H), δ 7.94 (s, 1H), δ 7.89 (t, 2H), δ 7.77 (d, 2H), δ 7.51 (d, 2H), δ 7.38 (t, 2H), δ 7.09 (t, 1H), δ 7.03 (d, 2H), δ 6.95 (t, 2H), δ 6.52 (s, 1H), δ 5.77 (d, 2H), δ 4.06 (t, 2H), δ 1.87 (s, 9H), δ 1.42 (t, 2H), δ 1.28 (s, 30H), δ 1.12 (s, 9H), δ 0.88 (t, 3H). 13C{1H} NMR, δ 187.40, δ 169.63, δ 161.73, δ 157.28, δ 153.26, δ 153.18, δ 149.05, δ 148.97, δ 147.16, δ 145.52, δ 139.68, δ 131.10, δ 129.14, δ 128.85, δ 128.13, δ 127.32, δ 126.18, δ 123.73, δ 120.58, δ 119.09, δ 115.28, δ 112.06, δ 102.20, δ 68.42, δ 35.96, δ 35.44, δ 31.89, δ 29.89, δ 29.68, δ 29.44, δ 29.32, δ 29.20, δ 28.87, δ 26.04, δ 22.65, δ 13.8. Elemental analysis calculated for [C₅₉H₇₆ClRuN₄O₂PF₆]: C, 61.37; H, 6.63; N, 4.85. Found: C, 61.23; H, 6.59; N, 4.54.

Other methods

DFT calculation. Complex 1 was optimized in its singlet, triplet, quintet, and septet electronic states employing B3LYP functional⁴⁵ with Grimme's D3 dispersion correction.⁴⁶ The SDD effective core potential (ECP) and associated basis set for Ru atom⁴⁷ were used and the 6-311G* basis set was used for all other atoms (Cl, O, N, C, and H).48 Solvent effects, (dichloromethane), were included in the calculations through polarizable continuum model (PCM).49 The ultrafine grid was used in the calculations. Vibrational frequency analysis was performed on optimized structures to confirm their convergence to the local minima at their respective potential energy surfaces. Natural orbital (NO) analysis was applied to determine the character of open-shell electronic states. AOMix program⁵⁰ was performed to determine the compositions of molecular orbitals and molecular fragments of the singlet ground state. Time-dependent density functional theory (TD-DFT)⁵¹ was employed for excited-state analysis, using the same level of theory as the ground state calculations. The stick spectrum was broadened using Lorentzian functions with a half-width at half-maximum (HWHM) of 0.12 eV. Solvent effects (dichloromethane) were included via the polarizable continuum model (PCM).

Half-wave potentials $(E_{1/2})$ were determined relative to the ferrocene/ferricenium (Fc/Fc⁺)redox couple through eqn (3):

$$E^{\circ}(\text{eV}) = -\frac{\Delta G_{\text{sol}}}{nF} - 5.00 \tag{3}$$

where $\Delta G_{\rm sol}$ is the change in solvated free energy upon reduction, n is the number of electrons (in this case, 1), and F is the Faraday constant. The specific reactions are the oxidation of Ru(III) complex (in singlet state) to Ru(IV) complex (in doublet state) and the reduction of Ru(III) complex (in singlet state) to Ru(0) complex (in doublet state). The calculated redox potentials are referenced to the Fc/Fc⁺ by subtracting the estimated absolute reduction potential of Fc/Fc⁺, 5.00 eV. All calculations were carried out using the Gaussian 16 software package (Revision A.03). All calculations

Formation of Pockels-Langmuir and Langmuir-Blodgett. An automated KSV Minitrough (Biolin, Espoo, Finland) was used to obtain the pressure vs. area (Π -A) isotherms at the air/water interphase. All experiments were performed at 23 ± 0.3 °C using ultra-pure water from a Barnstead Nanopure system as the subphase. Before the experiment, the impurities present at the surface of the aqueous subphase were removed by vacuum. The complex was dissolved in highly volatile dichloromethane solvent to prepare spreading solutions with a concentration of 1 mg mL⁻¹. Approximately 30-40 μL of spreading solution was introduced over the subphase for each trial and about 20 minutes waiting time was maintained before monolayer compression. The barriers were compressed at a rate of 10 mm min⁻¹ during each measurement and a paper Wilhelmy plate (20 × 10 mm) was used to measure the surface pressure of the isotherm. At least three reproducible measurements were recorded for the complex.

Brewster angle microscopy (BAM). The BAM micrographs of the complex was recorded using a CCD detector of KSV-Optrel BAM 300 with a HeNe laser (10 mW, 632.8 nm). The monolayer compression rate was maintained at 10 mm min⁻¹.

AFM measurements. Atomic force microscope images of the sample surfaces were taken using a Bruker Bioscope Catalyst AFM. A MicroMasch CSC 38 cantilever with a spring constant of 0.09 N m⁻¹ was used to image the surface in contact mode imaging in air. The cantilevers were cleaned with ethanol, followed by DI water before doing an experiment. The cleaned cantilever was then mounted on a cantilever holder, and the sum signal was maximized using the easy align system of the AFM. The AFM head was then placed on top of the AFM base plate where the prepared sample was placed. The cantilever was manually lowered carefully to approach the surface of the sample before engaging it automatically. The AFM hood was closed to avoid noises and vibrations from external factors, and the system was allowed to settle for about 5 minutes before starting the scan. All scanning was done with a scan rate of 1 Hz (10 μ m s⁻¹ tip velocity). For the roughness measurements, nine images of size 5 µm × 5 µm at nine different locations for each sample were taken and then cropped 2 μ m \times 2 μ m size images from the original 5 μ m \times 5 μm image for further analysis. The roughness analysis of the images was done using the NanoScope Analysis 1.5 software from Bruker. To measure the thickness of the coated layers, several scratches were made on the samples with a sharp blade. Scratches were then scanned in contact mode imaging in air and analyzed with the same software.

Measurement of I/V **curves.** Nano-scale devices were fabricated using gold-coated mica substrates covered with Langmuir–Blodgett monolayers of complex **1.** The top Au-electrode was coated on an EffaCoater gold sputter using the shadow masking method. The current–voltage (I/V) characteristics of the devices were measured using a Keithley 4200 semiconductor parameter analyser coupled to a Signatone S-1160 Probe Station at ambient conditions.

Author contributions

Samudra Amunugama: Methodology and writing of original draft, syntheses, spectroscopic analysis, junction fabrication. Eyram Asempa: Formal analysis of theoretical calculations and writing of original draft for DFT calculations. Ramesh Chandra Tripathi: Formal analysis of morphological characterization of films, thickness measurements of films, writing of methodology for AFM. Habib Baydoun: Formal analysis and methodology for X-ray diffraction. Dakshika Wanniarachchi: Synthesis and characterization of complex for X-ray analysis. Peter Hoffmann: Supervision of AFM morphological characterization. Elena Jakubikova: Formal analysis, supervision and writing of DFT section. Cláudio Verani: Overall conceptualization, formal analysis, data curation, funding acquisition, project administration, supervision, and manuscript revising and writing.

Conflicts of interest

There are no conflicts to declare.

Acknowledgements

The authors thankfully acknowledge the support from the National Science Foundation through the grant NSF-CHE1904584 to C. N. V., including financial support to S. A., and from the US Army Research Office under the contract W911NF-19-2-0194 to E. J. including financial support to E. A. A. We also acknowledge the use of the NCSU High-Performance Computing Center. Prof. Héctor Abruña at Cornell University is thanked for a discussion on the attribution of the electrochemical processes in 1.

Notes and references

- 1 C. N. Verani, Dalton Trans., 2018, 47, 14153-14168.
- 2 J. Park, A. N. Pasupathy, J. I. Goldsmith, C. Chang, Y. Yaish, J. R. Petta, M. Rinkoski, J. P. Sethna, H. D. Abruña and P. L. McEuen, *Nature*, 2002, 417, 722–725.
- 3 E. A. Osorio, K. Moth-Poulsen, H. S. van der Zant, J. Paaske, P. Hedegård, K. Flensberg, J. Bendix and T. Bjørnholm, *Nano Lett.*, 2010, **10**, 105–110.

4 Q. van Nguyen, U. Tefashe, P. Martin, M. L. Della Rocca, F. Lafolet, P. Lafarge, R. L. McCreery and J.-C. Lacroix, *Adv. Electron. Mater.*, 2020, **6**, 2070033.

- 5 K. Seo, A. V. Konchenko, J. Lee, G. S. Bang and H. Lee, J. Am. Chem. Soc., 2008, 130, 2553–2559.
- 6 J. Lee, H. Chang, S. Kim, G. S. Bang and H. Lee, Angew. Chem., Int. Ed., 2009, 48, 8501–8504.
- 7 D. Frath, V. Q. Nguyen, F. Lafolet, P. Martin and J.-C. Lacroix, *Chem. Commun.*, 2017, 53, 10997–11000.
- 8 (a) A. Aviram and M. A. Ratner, Chem. Phys. Lett., 1974, 29, 277–283; (b) R. M. Metzger, B. Chen, U. Höpfner, M. Lakshmikantham, D. Vuillaume, T. Kawai, X. Wu, H. Tachibana, T. V. Hughes and H. Sakurai, J. Am. Chem. Soc., 1997, 119, 10455–10466; (c) R. M. Metzger, Chem. Rev., 2015, 115, 5056–5115.
- (a) L. D. Wickramasinghe, M. M. Perera, L. Li, G. Mao, Z. Zhou and C. N. Verani, *Angew. Chem.*, 2013, 125, 13588–13592; (b) L. D. Wickramasinghe, S. Mazumder, S. Gonawala, M. M. Perera, H. Baydoun, B. Thapa, L. Li, L. Xie, G. Mao and Z. Zhou, *Angew. Chem., Int. Ed.*, 2014, 53, 14462–14467; (c) L. D. Wickramasinghe, S. Mazumder, K. K. Kpogo, R. J. Staples, H. B. Schlegel and C. N. Verani, *Chem. Eur. J.*, 2016, 22, 10786–10790; (d) A. I. Weeraratne, H. Baydoun, R. Shakya, J. Niklas, L. Xie, G. Mao, S. A. Stoian, O. G. Poluektov and C. N. Verani, *Dalton Trans.*, 2018, 47, 14352–14361.
- 10 (a) M. S. Johnson, L. Wickramasinghe, C. Verani and R. M. Metzger, *J. Phys. Chem. C*, 2016, **120**, 10578–10583;
 (b) M. S. Johnson, C. L. Horton, S. Gonawala, C. N. Verani and R. M. Metzger, *Dalton Trans.*, 2018, 47, 6344–6350.
- 11 L. Yuan, C. Franco, N. Crivillers, M. Mas-Torrent, L. Cao, C. Sangeeth, C. Rovira, J. Veciana and C. A. Nijhuis, *Nat. Commun.*, 2016, 7, 1–10.
- 12 P. Kornilovitch, A. Bratkovsky and R. S. Williams, *Phys. Rev. B: Condens. Matter Mater. Phys.*, 2002, **66**, 165436.
- 13 R. Liu, S.-H. Ke, W. Yang and H. U. Baranger, *J. Chem. Phys.*, 2006, **124**, 024718.
- 14 (a) D. C. Wanniarachchi, M. J. Heeg and C. N. Verani, *Inorg. Chem.*, 2014, 53, 3311–3319; (b) H. Chun, C. N. Verani, P. Chaudhuri, E. Bothe, E. Bill, T. Weyhermüller and K. Wieghardt, *Inorg. Chem.*, 2001, 40, 4157–4166; (c) P. Chaudhuri, C. N. Verani, E. Bill, E. Bothe, T. Weyhermüller and K. Wieghardt, *J. Am. Chem. Soc.*, 2001, 123, 2213–2223.
- 15 S. Maji, S. Patra, S. Chakraborty, D. Janardanan, S. M. Mobin, R. B. Sunoj and G. K. Lahiri, *Eur. J. Inorg. Chem.*, 2007, (2), 314–323.
- 16 S. Bonnet, J.-P. Collin, N. Gruber, J.-P. Sauvage and E. R. Schofield, *Dalton Trans.*, 2003, 4654–4662.
- 17 (a) M. Rupp, T. Auvray, E. Rousset, G. M. Mercier,
 V. Marvaud, D. G. Kurth and G. S. Hanan, *Inorg. Chem.*,
 2019, 58, 9127–9134; (b) F. Barigelletti, B. Ventura,
 J. P. Collin, R. Kayhanian, P. Gaviña and J. P. Sauvage,
 Eur. J. Inorg. Chem., 2000, 2000, 113–119; (c) M. I. Polson,
 E. A. Medlycott, G. S. Hanan, L. Mikelsons, N. J. Taylor,

- M. Watanabe, Y. Tanaka, F. Loiseau, R. Passalacqua and S. Campagna, *Chem. Eur. J.*, 2004, **10**, 3640–3648.
- 18 A. D. Chowdhury, A. Das, S. M. Mobin and G. K. Lahiri, *Inorg. Chem.*, 2011, **50**, 1775–1785.
- (a) J. Rochford, M.-K. Tsai, D. J. Szalda, J. L. Boyer, J. T. Muckerman and E. Fujita, *Inorg. Chem.*, 2010, 49, 860–869; (b) J. L. Boyer, J. Rochford, M.-K. Tsai, J. T. Muckerman and E. Fujita, *Coord. Chem. Rev.*, 2010, 254, 309–330; (c) S. Bhattacharya, P. Gupta, F. Basuli and C. G. Pierpont, *Inorg. Chem.*, 2002, 41, 5810–5816.
- 20 (a) R. Mukherjee, *Inorg. Chem.*, 2020, 59, 12961–12977;
 (b) A. Saha, A. Rajput, P. Gupta and R. Mukherjee, *Dalton Trans.*, 2020, 49, 15355–15375.
- 21 B. Siewert, M. Langerman, Y. Hontani, J. Kennis, V. Van Rixel, B. Limburg, M. Siegler, V. T. Saez, R. Kieltyka and S. Bonnet, *Chem. Commun.*, 2017, 53, 11126–11129.
- 22 (a) D. Lazić, A. Arsenijević, R. Puchta, Ž. D. Bugarčić and A. Rilak, *Dalton Trans.*, 2016, 45, 4633–4646; (b) A. Rilak, I. Bratsos, E. Zangrando, J. Kljun, I. Turel, Z. i. D. Bugarčić and E. Alessio, *Inorg. Chem.*, 2014, 53, 6113–6126.
- 23 R. Fernández-Terán and L. Sévery, *Inorg. Chem.*, 2020, 60, 1334–1343.
- 24 (a) T. Wada, K. Tsuge and K. Tanaka, *Inorg. Chem.*, 2001, 40, 329–337; (b) S. Bhattacharya, S. R. Boone, G. A. Fox and C. G. Pierpont, *J. Am. Chem. Soc.*, 1990, 112, 1088–1096; (c) H. Masui, A. Lever and P. R. Auburn, *Inorg. Chem.*, 1991, 30, 2402–2410; (d) M. Kurihara, S. Daniele, K. Tsuge, H. Sugimoto and K. Tanaka, *Bull. Chem. Soc. Jpn.*, 1998, 71, 867–875; (e) K. Tsuge, K. Tanaka, K. Tsuge, M. Kurihara and K. Tanaka, *Chem. Lett.*, 1998, 1998, 1069–1070; (f) M. Haga, E. S. Dodsworth and A. Lever, *Inorg. Chem.*, 1986, 25, 447–453.
- 25 A. Lever, P. R. Auburn, E. S. Dodsworth, M. A. Haga, W. Liu, M. Melnik and W. A. Nevin, *J. Am. Chem. Soc.*, 1988, 110, 8076–8084.
- 26 M.-K. Tsai, J. Rochford, D. E. Polyansky, T. Wada, K. Tanaka, E. Fujita and J. T. Muckerman, *Inorg. Chem.*, 2009, 48, 4372–4383.
- 27 F. D. Lesh, M. M. Allard, R. Shanmugam, L. M. Hryhorczuk, J. F. Endicott, H. B. Schlegel and C. N. Verani, *Inorg. Chem.*, 2011, 50, 969–977.
- 28 (a) M. Haga, E. S. Dodsworth, A. Lever, S. R. Boone and C. G. Pierpont, *J. Am. Chem. Soc.*, 1986, 108, 7413–7414;
 (b) M. W. Lynch, M. Valentine and D. N. Hendrickson, *J. Am. Chem. Soc.*, 1982, 104, 6982–6989.
- 29 (a) S. Bhattacharya, *Polyhedron*, 1994, 13, 451–456;
 (b) H. Sugimoto and K. Tanaka, *J. Organomet. Chem.*, 2001, 622, 280–285; (c) M. Ebadi and A. Lever, *Inorg. Chem.*, 1999, 38, 467–474; (d) N. Bag, A. Pramanik, G. K. Lahiri and A. Chakravorty, *Inorg. Chem.*, 1992, 31, 40–45.
- 30 The addition of the name Pockels to the films commonly known as Langmuir monolayers aims to rectify a historical omission towards the pioneering work of citizen scientist Ms Agnes Pockels (1862–1935) in the understanding of film formation at the air/water surface. See the following references: (a) L. Rayleigh and A. Pockels, *Nature*, 1891, 43, 437;

(b) A. Pockels, Nature, 1892, 46, 418-419; (c) A. Pockels, Nature, 1893, 48, 152-154; (d) A. Pockels, Nature, 1894, 50, 223-224.

- 31 G. Brezesinski, B. Dobner, C. Stefaniu and D. Vollhardt, Langmuir, 2011, 27, 5386-5392.
- 32 Y. Wang, X. Du, L. Guo and H. Liu, I. Chem. Phys., 2006, **124**, 134706.
- 33 T. Hama, A. Kouchi, N. Watanabe, S. Enami, T. Shimoaka and T. Hasegawa, J. Phys. Chem. B, 2017, 121, 11124-11131.
- 34 T. Leitner, J. Kattner and H. Hoffmann, Appl. Spectrosc., 2003, 57, 1502-1509.
- 35 (a) Z. Tang, R. K. Hicks, R. J. Magyar, S. Tretiak, Y. Gao and H.-L. Wang, Langmuir, 2006, 22, 8813-8820; (b) Z. Zhang, A. L. Verma, M. Yoneyama, K. Nakashima, K. Iriyama and Y. Ozaki, Langmuir, 1997, 13, 4422-4427.
- 36 R. M. Metzger, J. Mater. Chem., 2008, 18, 4364-4396.
- 37 K. Kitagawa, T. Morita and S. Kimura, Langmuir, 2005, 21, 10624-10631.
- 38 (a) J. He, O. Fu, S. Lindsay, J. W. Ciszek and J. M. Tour, J. Am. Chem. Soc., 2006, 128, 14828-14835; (b) N. Jaggi and D. Vij, in Handbook of Applied Solid State Spectroscopy, Springer, 2006, pp. 411-450; (c) L. Scudiero, D. E. Barlow and K. Hipps, J. Phys. Chem. B, 2002, 106, 996-1003; (d) A. Schmidt, N. Armstrong, C. Goeltner and K. Muellen, J. Phys. Chem., 1994, 98, 11780-11785.
- 39 (a) G. J. Ashwell, B. J. Robinson, M. A. Amiri, D. Locatelli, S. Quici and D. Roberto, J. Mater. Chem., 2005, 15, 4203-4205; (b) G. Jayamurugan, V. Gowri, D. Hernández, S. Martin, A. González-Orive, C. Dengiz, O. Dumele, F. Pérez-Murano, J. P. Gisselbrecht and C. Boudon, Chem. -Eur. J., 2016, 22, 10539-10547.
- 40 M. Souto, L. Yuan, D. C. Morales, L. Jiang, I. Ratera, C. A. Nijhuis and J. Veciana, J. Am. Chem. Soc., 2017, 139, 4262-4265.
- 41 L. Yuan, R. Breuer, L. Jiang, M. Schmittel and C. A. Nijhuis, Nano Lett., 2015, 15, 5506-5512.
- 42 (a) I. Hnid, A. Grempka, A. Khettabi, X. Sun, J. C. Lacroix, F. Lafolet and S. Cobo, J. Phys. Chem. C, 2020, 124, 26304-26309; (b) H. Atesci, V. Kaliginedi, J. A. C. Gil, H. Ozawa, J. M. Thijssen, P. Broekmann, M.-a. Haga and S. J. van der Molen, Nat. Nanotechnol., 2018, 13, 117-121; (c) Q. Van Nguyen, F. Lafolet, P. Martin and J. C. Lacroix, J. Phys. Chem. C, 2018, 122, 29069-29074.

- 43 R. R. Gagne, C. A. Koval and G. C. Lisensky, Inorg. Chem., 1980, 19, 2854-2855.
- 44 (a) C. B. Smith, C. L. Raston and A. N. Sobolev, Green Chem., 2005, 7, 650-654; (b) J. Wang and G. S. Hanan, Synlett, 2005, 1251-1254.
- 45 (a) A. D. Beck, I. Chem. Phys., 1993, 98, 5648-5646; (b) A. D. Becke, Phys. Rev. A, 1988, 38, 3098; (c) C. Lee, W. Yang and R. G. Parr, Phys. Rev. B: Condens. Matter Mater. Phys., 1988, 37, 785; (d) P. J. Stephens, F. J. Devlin, C. F. Chabalowski and M. J. Frisch, J. Phys. Chem., 1994, 98, 11623-11627.
- 46 S. Grimme, *I. Comput. Chem.*, 2006, 27, 1787-1799.
- 47 M. Kaupp, P. v. R. Schleyer, H. Stoll and H. Preuss, J. Chem. Phys., 1991, 94, 1360-1366.
- 48 R. Krishnan, J. S. Binkley, R. Seeger and J. A. Pople, J. Chem. Phys., 1980, 72, 650-654.
- 49 G. Scalmani and M. J. Frisch, J. Chem. Phys., 2010, 132, 114110.
- 50 (a) S. I. Gorelsky, AOMix: Program for molecular orbital analysis, https://www.sg-chem.net; (b) S. I. Gorelsky and A. B. P. Lever, J. Organomet. Chem., 2001, 635, 187-196.
- 51 M. E. Casida, C. Jamorski, K. C. Casida and D. R. Salahub, J. Chem. Phys., 1998, 108, 4439-4449.
- 52 H. M. Koepp, H. Wendt and H. Stkehlow, Z. Elektrochem., 1960, 64, 483-491.
- 53 M. J. Frisch, G. W. Trucks, H. B. Schlegel, G. E. Scuseria, M. A. Robb, J. R. Cheeseman, G. Scalmani, V. Barone, G. A. Petersson, H. Nakatsuji, X. Li, M. Caricato, A. V. Marenich, J. Bloino, B. G. Janesko, R. Gomperts, B. Mennucci, H. P. Hratchian, J. V. Ortiz, A. F. Izmaylov, J. L. Sonnenberg, D. Williams-Young, F. Ding, F. Lipparini, F. Egidi, J. Goings, B. Peng, A. Petrone, T. Henderson, D. Ranasinghe, V. G. Zakrzewski, J. Gao, N. Rega, G. Zheng, W. Liang, M. Hada, M. Ehara, K. Toyota, R. Fukuda, J. Hasegawa, M. Ishida, T. Nakajima, Y. Honda, O. Kitao, H. Nakai, T. Vreven, K. Throssell, J. A. Montgomery Jr., J. E. Peralta, F. Ogliaro, M. J. Bearpark, J. J. Heyd, E. N. Brothers, K. N. Kudin, V. N. Staroverov, T. A. Keith, R. Kobayashi, J. Normand, K. Raghavachari, A. P. Rendell, J. C. Burant, S. S. Iyengar, J. Tomasi, M. Cossi, J. M. Millam, M. Klene, C. Adamo, R. Cammi, J. W. Ochterski, R. L. Martin, K. Morokuma, O. Farkas, J. B. Foresman and D. J. Fox, Gaussian 16 Rev, 2016.